

The Raman Spectrum of Janus Transition Metal Dichalcogenide Monolayers WSSe and MoSSe

Marko M. Petrić,^{1,2,*} Malte Kremser,^{3,2,*} Matteo Barbone,^{1,2,*} Ying Qin,⁴ Yasir Sayyad,⁴ Yuxia Shen,⁴ Sefaattin Tongay,^{4,†} Jonathan J. Finley,^{3,2,‡} Andrés R. Botello-Méndez,^{5,§} and Kai Müller^{1,2,¶}

¹Walter Schottky Institut and Department of Electrical and Computer Engineering, Technische Universität München, Am Coulombwall 4, 85748 Garching, Germany

²Munich Center for Quantum Science and Technology (MCQST), Schellingstr. 4, 80799 Munich, Germany

³Walter Schottky Institut and Physik Department, Technische Universität München, Am Coulombwall 4, 85748 Garching, Germany

⁴Materials Science and Engineering, School for Engineering of Matter, Transport and Energy, Arizona State University, Tempe, Arizona 85287, USA

⁵Universidad Nacional Autónoma de México, Institute of Physics, 20-364, 01000 México, D.F., México

Janus transition metal dichalcogenides (TMDs) lose the horizontal mirror symmetry of ordinary TMDs, leading to the emergence of additional features, such as native piezoelectricity, Rashba effect, and enhanced catalytic activity. While Raman spectroscopy is an essential non-destructive, phase- and composition-sensitive tool to monitor the synthesis of materials, a comprehensive study of the Raman spectrum of Janus monolayers is still missing. Here, we discuss the Raman spectra of WSSe and MoSSe measured at room and cryogenic temperatures, near- and off-resonance. By combining Raman data with calculations of the phonon dispersion and using symmetry considerations, we identify the four first-order Raman modes and higher-order two-phonon modes. Moreover, we observe defect-activated phonon processes, which provide a route toward a quantitative assessment of the defect concentration and, thus, the crystal quality of the materials synthesized. Our work establishes a solid background for future research on material synthesis, study and application of Janus TMD monolayers.

INTRODUCTION

Over the past decade, TMD monolayers have emerged as a unique playground for exciton photophysics due to ~ 0.5 eV-high exciton binding energies [1, 2], strong light-matter interaction [3, 4], optically addressable valley-contrasting spin physics caused by broken inversion symmetry [5] and large spin-orbit coupling [6]. Further studies also revealed the presence of quantum light emitters [7–12] and evidence of strongly correlated phases such as superconductivity [13, 14], exciton and polaron Bose-Einstein condensation [15, 16]. Integrability on conventional silicon photonic technology [17, 18], large-area fabrication [19–21] and deterministic positioning of quantum emitters [22–24] widen the impact of TMDs to optoelectronics [25] and energy harvesting [26] as well as applications exploiting valleytronics [27, 28], spintronics [29–31], and quantum photonic properties [32, 33]. In addition, new functionalities and physical phenomena appear when stacking monolayers of TMDs on top of each other, forming artificial metamaterials held together by van der Waals forces [34]. Such heterostructures host long-lived, tuneable dipolar interlayer [35] and trapped moiré excitons [36–39], offering a rich playground for few- and many-body phenomena [40–46] placing them as candidates for a platform for solid-state quantum simulation [47].

In contrast to conventional, mirror-symmetric TMDs with stoichiometric formula MX_2 (where M is a transition metal and X is a chalcogen), Janus TMD monolayers

MXY are formed when the crystal plane of transition metal atoms is sandwiched between two planes each made of a different chalcogen atom X and Y . This breaks mirror symmetry along the direction perpendicular to the plane of the 2D material, reducing the overall symmetry of the crystal, and gives rise to an intrinsic electrical dipole in the unit cell created by the difference in electronegativity between top and bottom chalcogen atoms [48]. Consequently, theoretical studies predict the appearance of a multitude of physical phenomena such as piezoelectricity [49, 50], enhanced photocatalysis [51–54], Rashba splitting [55–57], and the presence of topological phases [58].

With first reports on the successful synthesis of Janus monolayers of MoSSe having appeared in 2017 [59, 60] and, to our knowledge, only one report of the growth of Janus monolayer WSSe as well as Janus heterostructure assembly [61], most of these effects are experimentally still largely unexplored. Inelastic light scattering is a powerful, non-destructive tool to gain insight into the structural and electronic properties of materials [62, 63]. Each Raman spectrum of 2D materials is a unique fingerprint of a sample, shedding light on its crystal and electronic band structure [64], layer number [65], interlayer coupling [66, 67], doping [68], defect density [69], electron-phonon interaction [70], etc. Moreover, Raman spectroscopy can be used in-situ during growth to distinguish a Janus monolayer from a disordered ternary alloy [71–74]. Thus, to synthesize high-quality Janus TMD crystals and unlock the predicted effects and applications it is crucial to have a detailed study of its vibrational

spectrum. However, a comprehensive study of the Raman spectrum of Janus monolayers WSSe and MoSSe is lacking. Initial experimental measurements have given limited insight on the Raman spectrum of Janus TMD monolayers, suffering from incomplete [59] or even incorrect [60] assignments of the first-order modes and leaving all other features unidentified.

In this work, we calculate the phonon band structure of Janus WSSe and MoSSe monolayers and their phonon density of states (PhDOS), which we use to predict the Raman modes and their energies. Then, we measure the Raman spectra of both materials at room and cryogenic (10 K) temperature and two excitation wavelengths λ_{ex} , closer to and farther from excitonic resonances. By comparing theory and experiments, we identify first-order Raman modes. As the experimental spectra show rich features arising beyond the calculated first-order processes, we then discuss the mechanisms of higher-order and defect-mediated Raman modes and assign them to the relevant experimental peaks.

RESULTS AND DISCUSSION

Standard TMD monolayers have D_{3h}^1 space group symmetry [75, 76], contrasting strongly with Janus TMD monolayers, for which rotation C_2 , improper rotation S_3 , and mirror σ_h symmetries are broken due to the different chalcogen atoms in the unit cell. This results in a lowering of the symmetry of the crystal to the symmorphic (i.e. all symmetry operations leave one common point fixed) C_{3v}^1 space group (C_{3v} point group). The unit cell of Janus monolayer MXY is formed from three atoms, resulting in $3 \times 3 = 9$ normal vibrational modes at the Γ point (centre) of the Brillouin Zone, of which three are acoustic and six are optical. Group theory identifies these vibrations as the irreducible representations of the C_{3v} point group, that can be expressed by $\Gamma_{C_{3v}}^{\text{vib}} = 3A_1(\Gamma_1) + 3E(\Gamma_3)$, where all of the modes are both Raman and infrared (IR) active. Here, $\Gamma_{C_{3v}}^{\text{vib}}$ is the irreducible representation of the total vibration, deduced from the underlying crystal symmetry using the C_{3v} character table (see **Supporting Information** (SI) Table S1). In-plane vibrations are defined as $E^{1,2}$ and out-of-plane as $A_1^{1,2}$, with $E^{1,2}$ being doubly degenerate at the Γ point (modes with the same symmetry are distinguished by the upper right corner index).

Owing to the conservation of energy and quasi-momentum \mathbf{q} in the crystal, first-order (i.e. one-phonon) scattering processes are bound to the Γ point of the Brillouin Zone due to the negligible photon momentum ($\mathbf{q} \approx 0$). The atomic displacements corresponding to the normal vibrational modes at Γ are schematically represented in Figure 1a with the transition metal atom in grey and the chalcogens Se and S in orange and yellow, respectively. We use density functional perturbation theory (DFPT) to predict the phonon modes (see **Methods**). In

WSSe at the Γ point they occur at 204 cm^{-1} , 282 cm^{-1} , 331 cm^{-1} , and 420 cm^{-1} (for E^1 , A_1^1 , E^2 , and A_1^2 , respectively). Analogously, in MoSSe at the Γ point they occur at 208 cm^{-1} , 293 cm^{-1} , 358 cm^{-1} , and 445 cm^{-1} (for E^1 , A_1^1 , E^2 , and A_1^2 , respectively). This can be seen in the phonon band structure of monolayer WSSe in Figure 1b and of monolayer MoSSe in Figure 1c. The three acoustic phonon branches correspond to the out-of-plane acoustic (ZA), the transverse acoustic (TA) and the in-plane longitudinal acoustic (LA) modes, respectively. The remaining six branches represent the out-of-plane optical (ZO_1 and ZO_2), the in-plane transverse optical (TO_1 and TO_2) and the in-plane longitudinal optical (LO_1 and LO_2) modes.

In addition to the Γ point, we further examine the vibrational modes at high symmetry points at the Brillouin Zone edge, \mathbf{K} and \mathbf{M} . At the \mathbf{K} point, the crystal exhibits C_3 point group symmetry with irreducible representation $\Gamma_{C_3}^{\text{vib}} = 3A(K_1) + 3^2E(K_2) \oplus 3^1E(K_3)$, where $^1E^{1,2,3}$, $^2E^{1,2,3}$, and $A^{1,2,3}$ are all Raman active modes. On the other hand, at the \mathbf{M} point, the crystal exhibits C_s point group symmetry with irreducible representation $\Gamma_{C_s}^{\text{vib}} = 6A'(M_1) + 3A''(M_2)$, where $A'^{1,2,3}$ and $A''^{1,2,3}$ are both Raman active modes. The character tables for different modes at Γ , \mathbf{K} , and \mathbf{M} are listed in SI Section S1. Accompanied to the phonon dispersion in Figure 1b and 1c, the phonon density of states (PhDOS) reveals a high density of phonons at the flat bands, in particular close to the high-symmetry points \mathbf{K} and \mathbf{M} , with all phonons being Raman active. The dispersion branches of WSSe in Figure 1b are energetically lower than the dispersion branches of MoSSe in Figure 1c, thus giving lower energy of phonons at the same point in the Brillouin Zone. This mainly occurs due to the larger atomic mass of W, which makes the vibrations softer, as in the case of regular Mo- and W-based TMDs [77]. The two materials also differ in the values of the phonon bandgaps (see SI Section S2).

We measured the Raman spectra of Janus TMD monolayers recorded from crystals grown via room temperature Selective Epitaxy Atomic Replacement (SEAR) [61], as described in the **Methods** section. Here, the top-layer selenium atoms, in already grown WSe₂ and MoSe₂ monolayers, are replaced by sulfur atoms, to eventually yield Janus TMD WSSe and MoSSe, respectively. WSSe was grown on Al₂O₃, whereas MoSSe was grown on a Si/SiO₂ substrate. We conduct Raman spectroscopy in a back-scattering configuration, with linearly polarized excitation and no polarization filtering of the Raman signal.

Figure 2 shows the Raman spectra of Janus monolayer WSSe and MoSSe between 100 and 500 cm^{-1} , collected with a laser excitation wavelength λ_{ex} of 532 nm (green curves) and 633 nm (red curves), above the excitonic bandgap at 10 K of both WSSe [61] ($\sim 670 \text{ nm}$) and MoSSe [59–61] ($\sim 710 \text{ nm}$) (see SI Figure S2). Figure 2a and 2b, show typical Raman spectra recorded from

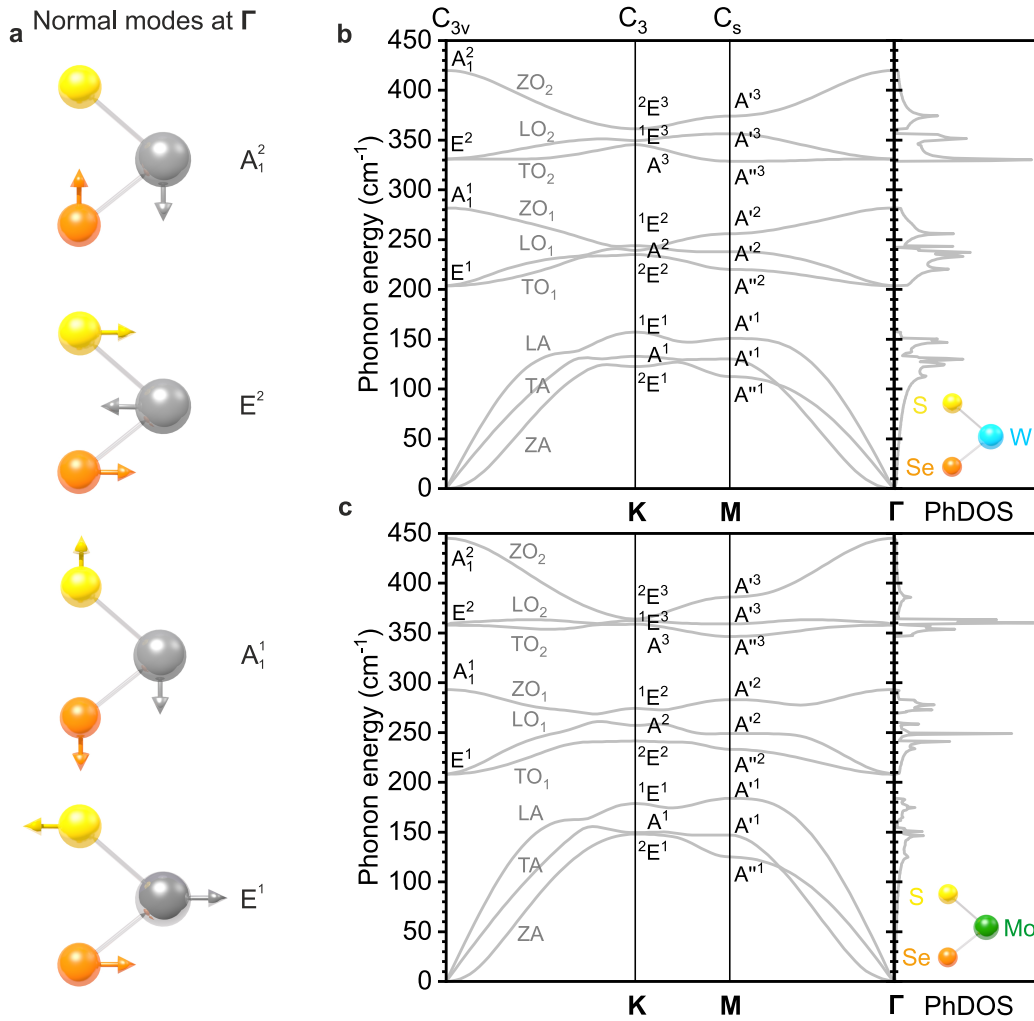


FIGURE 1. **First-order phonons and phonon band structure of Janus TMD monolayer WSSe and MoSSe.** (a) Schematic representation of the atomic vibrations at the center Γ of the Brillouin Zone. Transition metal, selenium and sulfur atoms are identified by grey, orange, and yellow, respectively. DFPT calculations of the phonon band structure of WSSe ((b), left panel) and MoSSe ((c), left panel). Each energy dispersion diagram shows three acoustic (ZA, TA, LA) and six optical (ZO₁, ZO₂, TO₁, TO₂, LO₁, LO₂) phonon branches. The corresponding PhDOS are shown in (b) and (c) (right panels). Vibrational modes are labeled at the high-symmetry points Γ ($E^{1,2}, A_1^{1,2}$), K (${}^1E^{1,2,3}, {}^2E^{1,2,3}, A_1^{1,2,3}$), and M ($A^{1,2,3}, A^{''1,2,3}$).

Janus monolayer WSSe at room and cryogenic temperatures, respectively. From the comparison of Raman spectra at 10 K with the calculated PhDOS in Figure 2b and 2c, where the dashed blue lines indicate the calculated values of Γ phonons, we assign the first-order Raman modes E^1 at $\sim 208 \text{ cm}^{-1}$ for $\lambda_{\text{ex}} = 633 \text{ nm}$ ($\sim 211 \text{ cm}^{-1}$ for $\lambda_{\text{ex}} = 532 \text{ nm}$), A_1^1 at $\sim 287 \text{ cm}^{-1}$ ($\sim 289 \text{ cm}^{-1}$), E^2 at $\sim 337 \text{ cm}^{-1}$ ($\sim 339 \text{ cm}^{-1}$), and A_1^2 at $\sim 426 \text{ cm}^{-1}$ ($\sim 429 \text{ cm}^{-1}$). All predicted first-order Raman modes, indicated in the spectra by blue arrows, are visible in all experimental conditions, albeit their intensity is maximum at 10 K and for $\lambda_{\text{ex}} = 633 \text{ nm}$, which is close to A exciton resonance (top valence band to conduction band, see SI Figure S2). The experimental results closely match the theoretical predictions. For the spectra ac-

quired at $\lambda_{\text{ex}} = 633 \text{ nm}$, we observe a broad background signal above $\sim 350 \text{ cm}^{-1}$, stemming from the photoluminescence tail of the material, due to the energetic proximity to the exciton transition. The Raman peaks E^1 at $\sim 204 \text{ cm}^{-1}$ and A_1^2 at $\sim 420 \text{ cm}^{-1}$ appear to be asymmetric, which can be attributed to phonon confinement effects due to imperfect crystal quality [78, 79]. The experimental spectra also reveal a peak at $\sim 154 \text{ cm}^{-1}$, as indicated by grey arrows, which is especially strong at 10 K and $\lambda_{\text{ex}} = 532 \text{ nm}$, and corresponds to the position of the A_1^1 mode in the LA branch at the M point. This mode is expected to be silent in first-order Raman processes since its $|\mathbf{q}| > 0$. We can exclude that this peak is caused by higher-order Raman modes due to its low energy and, therefore, attribute its appearance to defect-

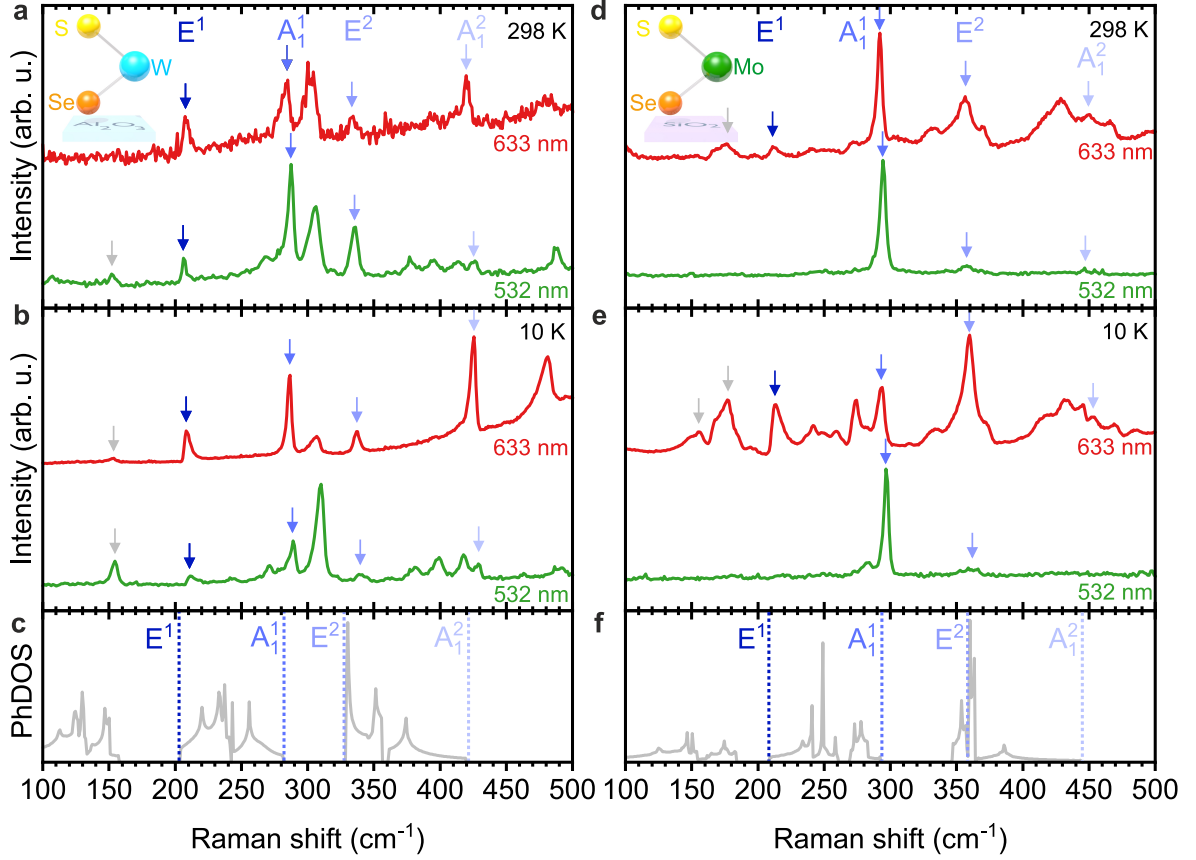


FIGURE 2. **Raman spectra of Janus TMD monolayers and first-order phonon modes.** (a) Room temperature and (b) 10 K Raman spectra of WSSe at $\lambda_{\text{ex}} = 532$ nm (green curves) and $\lambda_{\text{ex}} = 633$ nm (red curves). Blue and grey arrows indicate first-order and defect-activated Raman modes, respectively. (c) PhDOS of WSSe, with the calculated positions of the first-order Raman modes identified by dashed blue lines. (d)-(e) Corresponding Raman spectra and (f) PhDOS with predicted first-order Raman modes of MoSSe.

activation that relaxes the $\mathbf{q} \approx 0$ selection rule [69, 80].

The Raman spectra of Janus monolayer MoSSe are presented in Figure 2d-f, accompanied by the calculated PhDOS. Analogously to Janus monolayer WSSe, we compare the spectra to the theoretically predicted phonon energies (Figure 2f, dashed blue lines) and assign the first-order Raman modes E^1 at ~ 214 cm^{-1} for $\lambda_{\text{ex}} = 633$ nm, A_1^1 at ~ 294 cm^{-1} (~ 297 cm^{-1} for $\lambda_{\text{ex}} = 532$ nm), E^2 at ~ 360 cm^{-1} (~ 361 cm^{-1}), and A_1^2 at ~ 453 cm^{-1} . Here, the spectra are strongly affected by the λ_{ex} . First-order Raman modes, indicated by the blue arrows, are all visible only at $\lambda_{\text{ex}} = 633$ nm, while barely two peaks are visible at $\lambda_{\text{ex}} = 532$ nm. This arises once $\lambda_{\text{ex}} = 633$ nm (1.96 eV) is close to the B exciton transition (bottom valence band to conduction band, see SI Figure S2), thereby increasing the Raman cross-section. Again, we generally observe good agreement between theory and experiment, well within the ~ 8 cm^{-1} error of the calculations. Also for MoSSe, peaks appear around ~ 150 cm^{-1} and ~ 180 cm^{-1} for $\lambda_{\text{ex}} = 633$ nm, as indicated by grey arrows, whose intensity is enhanced at 10 K. Similar to

WSSe, the energy of the peaks in the ~ 150 cm^{-1} range corresponds to the A^1 mode in the TA branch at the \mathbf{M} point and to the A^1 and ${}^2E^1$ modes in the TA, ZA branches at the \mathbf{K} point. The peaks in the ~ 180 cm^{-1} range correspond to the A^1 mode in the LA branch at the \mathbf{M} point and the ${}^1E^1$ mode at the \mathbf{K} point in the LA branch. As discussed above, we exclude these peaks to be the result of higher-order Raman transitions due to their low energy, and we attribute their appearance to defect-activation. Interestingly, the presence of defect-activated Raman modes can be used to monitor the defect concentration in the crystal, in analogy to the D peak in graphene [80], and as such constitutes precious information to assess crystal quality. The peak at ~ 274 cm^{-1} corresponds to the ${}^1E^2$ mode in the first ZO branch at \mathbf{K} , however, due to the presence of other non-double-resonant phonon combinations matching the same energy, its assignment requires further investigation. For completeness, all first-order Raman modes at $\mathbf{\Gamma}$ are summarized in Table 1.

To explore higher-order Raman peaks, we plot the Ra-

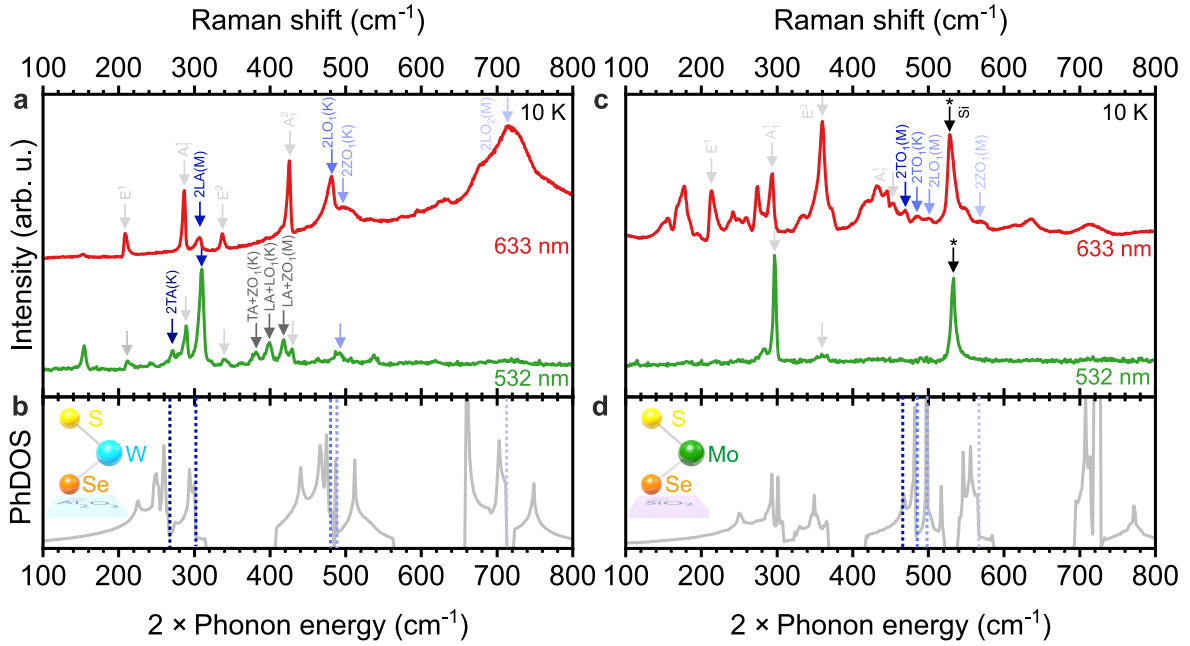


FIGURE 3. **Higher-order Raman processes in Janus WSe and MoSSe monolayers.** Raman spectra of (a) WSe and (c) MoSSe at $\lambda_{\text{ex}} = 532$ nm (green curves) and $\lambda_{\text{ex}} = 633$ nm (red curves). Blue-shaded arrows indicate Raman peaks corresponding to double-resonant processes with mode assignments following Table 2. Defect-assisted processes are indicated by dark grey. For comparison, light grey denotes first-order modes. All measurements are taken at 10 K. Black arrows indicate Raman signal of the substrate. PhDOS of double-resonant phonon modes of (b) WSe and (d) MoSSe. Dotted lines indicate energies of double-resonant phonons that correspond to observed Raman peaks indicated by the same color.

λ_{exc}	Phonon mode	WSe (cm^{-1})			MoSSe (cm^{-1})		
		298 K	10 K	Theory	298 K	10 K	Theory
633 nm	E^1	207	208	204	212	214	208
	A_1^1	285	287	282	292	294	293
	E^2	334	337	331	357	360	358
	A_1^2	420	426	420	450	453	445
532 nm	E^1	206	211	204	-	-	208
	A_1^1	288	289	282	294	297	293
	E^2	336	339	331	358	361	358
	A_1^2	426	429	420	447	-	445

TABLE 1. **List of first-order Raman modes of Janus monolayers WSe and MoSSe at all measured experimental conditions and comparison with the DFPT calculations.**

man spectra of Janus monolayers WSe and MoSSe at 10 K between 100 and 800 cm^{-1} (Figure 3a and 3c) and compare them to twice the phonon energy of the PhDOS (Figure 3b and 3d). This is motivated by the role of double-resonant Raman scattering [81] in higher-order Raman transitions. In double-resonant Raman scattering, two phonons with the same momentum but opposite direction make electrons scatter far from their excitation point in the Brillouin Zone and then come back to the initial position, through two resonant and two non-resonant scattering events, satisfying $\mathbf{q} \approx 0$. Double-resonant Raman processes in WSe and MoSSe are indicated by blue

arrows in Figure 3a and 3c. Higher-order scattering processes that include phonons from different branches are also energetically allowed through defect activation that locally break crystal symmetries (dark grey arrows). A comprehensive assignment list of the observed higher-order Raman peaks is given in Table 2. The unassigned peaks which do not match with double-resonant processes may be defect-activated, however, further studies are required to elucidate their nature.

WSe		MoSSe	
Peak (cm^{-1})	Assignments	Peak (cm^{-1})	Assignments
271 [†]	2TA(K)	476	2TO ₁ (M)
307	2LA(M)	486	2TO ₁ (K)
382 [†]	TA+ZO ₁ (K)	501	2LO ₁ (M)
399 [†]	LA+LO ₁ (K)	569	2ZO ₁ (M)
418 [†]	LA+ZO ₁ (M)		
481	2LO ₁ (K)		
495	2ZO ₁ (K)		
714	2LO ₂ (M)		

TABLE 2. **List of higher-order Raman modes of Janus monolayers WSe and MoSSe, listed by experimental energy from spectra collected at $\lambda_{\text{ex}} = 633$ nm ([†] $\lambda_{\text{ex}} = 523$ nm) and 10 K.**

CONCLUSION

In summary, we presented a combined theoretical and experimental study of Raman modes of Janus monolayers WSSe and MoSSe. Excellent agreement was found for the frequencies of first- and higher-order Raman modes. Moreover, we discovered the presence of defect-activation of otherwise silent Raman modes, which may be used as markers for assessing crystal quality in further studies.

The recent synthesis of Janus monolayer TMDs adds an extra degree of freedom to the wider family of two-dimensional and layered materials, with the presence of tuneable, strongly interacting dipolar excitons in single-layer materials as the stepping-stone for further exploration of correlated many-body states, exciton transport and applications that exploit such features. However, novel physics and exciting new applications require in-depth information over materials' properties and growth quality, with Raman spectroscopy being a widely utilized technique in such regard due to its descriptive power and simplicity of use and interpretation. Our work sets a general and much-needed reference over the vibrational properties of Janus monolayers, provides a starting point for further investigations on the role of phonons in such materials and enables the benchmarking of future crystal growth attempts.

METHODS

DFPT

Phonon dispersion relations were calculated using density functional perturbation theory with the local-density approximation to the exchange-correlation function [82, 83]. The vacuum distance between neighboring layers was 20 Å to describe isolated layers within the periodic boundary conditions. Norm-conserving pseudopotentials and a basis set defined from a energy cutoff of 105 Ry [84, 85] were used. The first Brillouin Zone was sampled with a 15×15×1 Monkhorst Pack grid.

SEAR

The synthesis of Janus TMDs is carried out in a specially designed quartz chamber, and a home built inductively coupled plasma system. The plasma chamber consists of a 5-foot long quartz tube with a 1-inch inner diameter suspended off-centered on a Lindberg Blue/M single-zone furnace. A copper coil with a length ~1.5 inches consisting of about five turns were wound around the quartz tube. The end of the Cu coil is connected to a 100 W tunable RF source (SEREN R101) through a custom-designed impedance match network. One end of the quartz tube is connected to an Edwards vacuum pump

while the other end is fitted with a hydrogen supply line, hydrogen flow rate and the pressure within the chamber is regulated by means of a capacitance manometer and a pressure controller. For the synthesis of Janus TMDs, the reaction chamber is pumped down to a base pressure of 15 mTorr, after which the chamber was purged with 20 sccm H₂ flow, maintaining an operation pressure at 300 mTorr. Plasma was generated with 15 W RF power, and the visible plasma tail position was marked on the quartz tube. For the SEAR process to create WSSe, CVD grown WSe₂ was placed 4 cm upstream of marked visible plasma tail position onto a quartz boat, and 2 g sulfur was placed 15 cm upstream of the H₂ plasma tail. Plasma treatment lasted for 18 min. For the creation of MoSSe, the position of CVD-grown MoSe₂ and S source were kept at the same position as WSSe, except the processing time was decreased to 8 min because of the lower Mo-Se bond energy. The SEAR process can also be set up to create a 2D Janus structure from sulfur-based TMDs and selenium precursors in a similar fashion by varying the processing parameters.

Optical Setup

Raman and PL measurements were done using a custom-made confocal microscope in back-scattering geometry. The excitation laser beam is focused on the sample by an objective with N.A. = 0.75 to a diffraction-limited spot. For cryogenic measurements a He-flow cryostat (Cryovac) was used. The collected light is analyzed in a spectrometer (maximum point-to-point resolution ~1.2 cm⁻¹ with a grating 1200/mm lines) coupled to a Charged-Coupled Device (Horiba). Both incident (\mathbf{e}_i) and scattered (\mathbf{e}_s) light polarization vectors are placed in the xy -plane, which is relevant to account for the Raman intensity $I = |\mathbf{e}_s R \mathbf{e}_i|^2$ (for the case of no polarization filtering in the detection path, $I = |R \mathbf{e}_i|^2$) [63]. Here, R represents the Raman tensor, which is derived from the point group symmetry, and alongside the scattering configuration dictates the selection rules [86, 87] (see SI Table S4).

ACKNOWLEDGEMENTS

We thank Moritz Meyer for technical assistance. S.T. acknowledges support from NSF DMR-1955889, NSF CMMI-1933214, and NSF DMR-1552220. K.M. and J.J.F. acknowledge support from the European Union Horizon 2020 research and innovation programme under grant agreement No. 820423 (S2QUIP) and the Deutsche Forschungsgemeinschaft (DFG, German Research Foundation) under Germany's Excellence Strategy – MCQST (EXC-2111) and e-Conversion (EXC-2089). M.M.P. acknowledges TUM International Gradu-

ate School of Science and Engineering (IGSSE). M.K. acknowledges support from the International Max Planck Research School for Quantum Science and Technology (IMPRS-QST). M.B. acknowledges support from the Alexander von Humboldt Foundation. K.M. acknowledges support from the Bavarian Academy of Sciences and Humanities. A.R.B.-M. acknowledges support from DGTIC-UNAM Supercomputing Center under Project LANCAD-UNAM-DGTIC-359.

AUTHOR CONTRIBUTIONS

M.M.P., M.K., and M.B. contributed equally to this work. M.B., J.J.F., A.R.B.-M., and K.M. conceived and managed the project. Y.Q., Y.Sa., Y.Sh., and S.T. grew Janus TMD monolayers. M.M.P., M.K., and M.B. performed the optical measurements and analyzed the data. A.R.B.-M. performed DFPT calculations. All authors participated in the discussion of the results and the writing of the manuscript.

ADDITIONAL INFORMATION

Supporting Information

Supporting information that accompanies this work: Symmetry and character tables; Phonon bandgaps; Photoluminescence of WSSe and MoSSe.

Notes

The authors declare no competing financial interest.

* These authors contributed equally to this work.

† Sefaattin.Tongay@asu.edu

‡ finley@wsi.tum.de

§ botello@fisica.unam.mx

¶ Kai.Mueller@wsi.tum.de

- [1] A. Chernikov, T. C. Berkelbach, H. M. Hill, A. Rigosi, Y. Li, O. B. Aslan, D. R. Reichman, M. S. Hybertsen, and T. F. Heinz, *Physical Review Letters* **113**, 076802 (2014).
- [2] G. Wang, A. Chernikov, M. M. Glazov, T. F. Heinz, X. Marie, T. Amand, and B. Urbaszek, *Reviews of Modern Physics* **90**, 673 (2018).
- [3] M. Bernardi, M. Palummo, and J. C. Grossman, *Nano Letters* **13**, 3664 (2013).
- [4] U. Wurstbauer, B. Miller, E. Parzinger, and A. W. Holleitner, *Journal of Physics D: Applied Physics* **50**, 173001 (2017).
- [5] D. Xiao, G.-B. Liu, W. Feng, X. Xu, and W. Yao, *Physical Review Letters* **108** (2012), 10.1103/PhysRevLett.108.196802.
- [6] Z. Y. Zhu, Y. C. Cheng, and U. Schwingenschlögl, *Physical Review B* **84**, 78 (2011).
- [7] P. Tonndorf, R. Schmidt, R. Schneider, J. Kern, M. Buscema, G. A. Steele, A. Castellanos-Gomez, H. S. J. van der Zant, S. Michaelis de Vasconcellos, and R. Bratschitsch, *Optica* **2**, 347 (2015).
- [8] M. Koperski, K. Nogajewski, A. Arora, V. Cherkez, P. Mallet, J.-Y. Veuillen, J. Marcus, P. Kossacki, and M. Potemski, *Nature Nanotechnology* **10**, 503 (2015).
- [9] A. Srivastava, M. Sidler, A. V. Allain, D. S. Lembke, A. Kis, and A. Imamoglu, *Nature Nanotechnology* **10**, 491 (2015).
- [10] C. Chakraborty, L. Kinnischtzke, K. M. Goodfellow, R. Beams, and A. N. Vamivakas, *Nature Nanotechnology* **10**, 507 (2015).
- [11] Y.-M. He, G. Clark, J. R. Schaibley, Y. He, M.-C. Chen, Y.-J. Wei, X. Ding, Q. Zhang, W. Yao, X. Xu, C.-Y. Lu, and J.-W. Pan, *Nature Nanotechnology* **10**, 497 (2015).
- [12] C. Palacios-Berraquero, M. Barbone, D. M. Kara, X. Chen, I. Goykhman, D. Yoon, A. K. Ott, J. Beitner, K. Watanabe, T. Taniguchi, A. C. Ferrari, and M. Atatüre, *Nature Communications* **7**, 12978 (2016).
- [13] J. T. Ye, Y. J. Zhang, R. Akashi, M. S. Bahramy, R. Arita, and Y. Iwasa, *Science* **338**, 1193 (2012).
- [14] D. Costanzo, S. Jo, H. Berger, and A. F. Morpurgo, *Nature Nanotechnology* **11**, 339 (2016).
- [15] O. Cotlet, S. Zeytinoglu, M. Sigrist, E. Demler, and A. Imamoglu, *Physical Review B* **93**, 996 (2016).
- [16] A. Kogar, M. S. Rak, S. Vig, A. A. Husain, F. Flicker, Y. I. Joe, L. Venema, G. J. MacDougall, T. C. Chiang, E. Fradkin, J. van Wezel, and P. Abbamonte, *Science* **358**, 1314 (2017).
- [17] P. Tonndorf, O. Del Pozo-Zamudio, N. Gruhler, J. Kern, R. Schmidt, A. I. Dmitriev, A. P. Bakhtinov, A. I. Tartakovskii, W. Pernice, S. Michaelis de Vasconcellos, and R. Bratschitsch, *Nano Letters* **17**, 5446 (2017).
- [18] N. Youngblood and M. Li, *Nanophotonics* **6**, 892 (2017).
- [19] Y.-H. Lee, X.-Q. Zhang, W. Zhang, M.-T. Chang, C.-T. Lin, K.-D. Chang, Y.-C. Yu, J. T.-W. Wang, C.-S. Chang, L.-J. Li, and T.-W. Lin, *Advanced Materials* **24**, 2320 (2012).
- [20] Y. Zhan, Z. Liu, S. Najmaei, P. M. Ajayan, and J. Lou, *Small* **8**, 966 (2012).
- [21] Y.-H. Lee, L. Yu, H. Wang, W. Fang, X. Ling, Y. Shi, C.-T. Lin, J.-K. Huang, M.-T. Chang, C.-S. Chang, M. Dresselhaus, T. Palacios, L.-J. Li, and J. Kong, *Nano Letters* **13**, 1852 (2013).
- [22] C. Palacios-Berraquero, D. M. Kara, A. R.-P. Montblanch, M. Barbone, P. Latawiec, D. Yoon, A. K. Ott, M. Loncar, A. C. Ferrari, and M. Atatüre, *Nature Communications* **8**, 15093 (2017).
- [23] A. Branny, S. Kumar, R. Proux, and B. D. Gerardot, *Nature Communications* **8**, 15053 (2017).
- [24] J. Klein, M. Lorke, M. Florian, F. Sigger, L. Sigl, S. Rey, J. Wierzbowski, J. Cerne, K. Müller, E. Mitterreiter, P. Zimmermann, T. Taniguchi, K. Watanabe, U. Wurstbauer, M. Kaniber, M. Knap, R. Schmidt, J. J. Finley, and A. W. Holleitner, *Nature Communications* **10**, 2755 (2019).
- [25] J. S. Ross, P. Klement, A. M. Jones, N. J. Ghimire, J. Yan, D. G. Mandrus, T. Taniguchi, K. Watanabe, K. Kitamura, W. Yao, D. H. Cobden, and X. Xu, *Nature Nanotechnology* **9**, 268 (2014).

- [26] A. Pospischil, M. M. Furchi, and T. Mueller, *Nature Nanotechnology* **9**, 257 (2014).
- [27] A. M. Jones, H. Yu, N. J. Ghimire, S. Wu, G. Aivazian, J. S. Ross, B. Zhao, J. Yan, D. G. Mandrus, Di Xiao, W. Yao, and X. Xu, *Nature Nanotechnology* **8**, 634 (2013).
- [28] X. Xu, W. Yao, Di Xiao, and T. F. Heinz, *Nature Physics* **10**, 343 (2014).
- [29] K. F. Mak, K. L. McGill, J. Park, and P. L. McEuen, *Science* **344**, 1489 (2014).
- [30] W. Yan, O. Txoperena, R. Llopis, H. Dery, L. E. Hueso, and F. Casanova, *Nature Communications* **7**, 13372 (2016).
- [31] W. Han, *APL Materials* **4**, 032401 (2016).
- [32] M. Atatüre, D. Englund, N. Vamivakas, S.-Y. Lee, and J. Wrachtrup, *Nature Reviews Materials* **3**, 38 (2018).
- [33] I. Aharonovich, D. Englund, and M. Toth, *Nature Photonics* **10**, 631 (2016).
- [34] A. K. Geim and I. V. Grigorieva, *Nature* **499**, 419 (2013).
- [35] P. Rivera, J. R. Schaibley, A. M. Jones, J. S. Ross, S. Wu, G. Aivazian, P. Klement, K. Seyler, G. Clark, N. J. Ghimire, J. Yan, D. G. Mandrus, W. Yao, and X. Xu, *Nature Communications* **6**, 6242 (2015).
- [36] K. L. Seyler, P. Rivera, H. Yu, N. P. Wilson, E. L. Ray, D. G. Mandrus, J. Yan, W. Yao, and X. Xu, *Nature* **567**, 66 (2019).
- [37] C. Jin, E. C. Regan, A. Yan, M. Iqbal Bakti Utama, D. Wang, S. Zhao, Y. Qin, S. Yang, Z. Zheng, S. Shi, K. Watanabe, T. Taniguchi, S. Tongay, A. Zettl, and F. Wang, *Nature* **567**, 76 (2019).
- [38] K. Tran, G. Moody, F. Wu, X. Lu, J. Choi, K. Kim, A. Rai, D. A. Sanchez, J. Quan, A. Singh, J. Embbley, A. Zepeda, M. Campbell, T. Autry, T. Taniguchi, K. Watanabe, N. Lu, S. K. Banerjee, K. L. Silverman, S. Kim, E. Tutuc, L. Yang, A. H. MacDonald, and X. Li, *Nature* **567**, 71 (2019).
- [39] E. M. Alexeev, D. A. Ruiz-Tijerina, M. Danovich, M. J. Hamer, D. J. Terry, P. K. Nayak, S. Ahn, S. Pak, J. Lee, J. I. Sohn, M. R. Molas, M. Koperski, K. Watanabe, T. Taniguchi, K. S. Novoselov, R. V. Gorbachev, H. S. Shin, V. I. Fal'ko, and A. I. Tartakovskii, *Nature* **567**, 81 (2019).
- [40] K. F. Mak, K. He, C. Lee, G. H. Lee, J. Hone, T. F. Heinz, and J. Shan, *Nature Materials* **12**, 207 (2013).
- [41] M. Barbone, A. R.-P. Montblanch, D. M. Kara, C. Palacios-Berraquero, A. R. Cadore, D. de Fazio, B. Pingault, E. Mostaani, H. Li, B. Chen, K. Watanabe, T. Taniguchi, S. Tongay, G. Wang, A. C. Ferrari, and M. Atatüre, *Nature Communications* **9**, 3721 (2018).
- [42] Z. Li, T. Wang, Z. Lu, C. Jin, Y. Chen, Y. Meng, Z. Lian, T. Taniguchi, K. Watanabe, S. Zhang, D. Smirnov, and S.-F. Shi, *Nature Communications* **9**, 3719 (2018).
- [43] Z. Ye, L. Waldecker, E. Y. Ma, D. Rhodes, A. Antony, B. Kim, X.-X. Zhang, M. Deng, Y. Jiang, Z. Lu, D. Smirnov, K. Watanabe, T. Taniguchi, J. Hone, and T. F. Heinz, *Nature Communications* **9**, 3718 (2018).
- [44] S.-Y. Chen, T. Goldstein, T. Taniguchi, K. Watanabe, and J. Yan, *Nature Communications* **9**, 3717 (2018).
- [45] K. Hao, J. F. Specht, P. Nagler, L. Xu, K. Tran, A. Singh, C. K. Dass, C. Schüller, T. Korn, M. Richter, A. Knorr, X. Li, and G. Moody, *Nature Communications* **8**, 15552 (2017).
- [46] M. Kremser, M. Brotons-Gisbert, J. Knörzer, J. Gückelhorn, M. Meyer, M. Barbone, A. V. Stier, B. D. Gerardot, K. Müller, and J. J. Finley, *npj 2D Materials and Applications* **4**, 6242 (2020).
- [47] F. Wu, T. Lovorn, E. Tutuc, and A. H. MacDonald, *Physical Review Letters* **121**, 026402 (2018).
- [48] F. Li, W. Wei, P. Zhao, B. Huang, and Y. Dai, *The Journal of Physical Chemistry Letters* **8**, 5959 (2017).
- [49] L. Dong, J. Lou, and V. B. Shenoy, *ACS Nano* **11**, 8242 (2017).
- [50] Y. Guo, S. Zhou, Y. Bai, and J. Zhao, *Applied Physics Letters* **110**, 163102 (2017).
- [51] D. Er, H. Ye, N. C. Frey, H. Kumar, J. Lou, and V. B. Shenoy, *Nano Letters* **18**, 3943 (2018).
- [52] Z. Guan, S. Ni, and S. Hu, *The Journal of Physical Chemistry C* **122**, 6209 (2018).
- [53] Y. Ji, M. Yang, H. Lin, T. Hou, L. Wang, Y. Li, and S.-T. Lee, *The Journal of Physical Chemistry C* **122**, 3123 (2018).
- [54] C. Xia, W. Xiong, J. Du, T. Wang, Y. Peng, and J. Li, *Physical Review B* **98** (2018), 10.1103/PhysRevB.98.165424.
- [55] Y. C. Cheng, Z. Y. Zhu, M. Tahir, and U. Schwingenschlögl, *EPL (Europhysics Letters)* **102**, 57001 (2013).
- [56] T. Hu, F. Jia, G. Zhao, J. Wu, A. Stroppa, and W. Ren, *Physical Review B* **97**, 78 (2018).
- [57] Q.-F. Yao, J. Cai, W.-Y. Tong, S.-J. Gong, J.-Q. Wang, X. Wan, C.-G. Duan, and J. H. Chu, *Physical Review B* **95** (2017), 10.1103/PhysRevB.95.165401.
- [58] Y. Ma, L. Kou, B. Huang, Y. Dai, and T. Heine, *Physical Review B* **98** (2018), 10.1103/PhysRevB.98.085420.
- [59] A.-Y. Lu, H. Zhu, J. Xiao, C.-P. Chuu, Y. Han, M.-H. Chiu, C.-C. Cheng, C.-W. Yang, K.-H. Wei, Y. Yang, Y. Wang, D. Sokaras, D. Nordlund, P. Yang, D. A. Muller, M.-Y. Chou, X. Zhang, and L.-J. Li, *Nature Nanotechnology* **12**, 744 (2017).
- [60] J. Zhang, S. Jia, I. Kholmanov, L. Dong, D. Er, W. Chen, H. Guo, Z. Jin, V. B. Shenoy, L. Shi, and J. Lou, *ACS Nano* **11**, 8192 (2017).
- [61] D. B. Trivedi, G. Turgut, Y. Qin, M. Y. Sayyad, D. Hajar, M. Howell, L. Liu, S. Yang, M. M. Petrić, M. Meyer, M. Kremser, M. Barbone, G. Soavi, A. V. Stier, J. J. Finley, H. Zhuang, K. Müller, and S. Tongay, (submitted) (2020).
- [62] X. Zhang, X.-F. Qiao, W. Shi, J.-B. Wu, D.-S. Jiang, and P.-H. Tan, *Chemical Society Reviews* **44**, 2757 (2015).
- [63] R. Saito, Y. Tatsumi, S. Huang, X. Ling, and M. S. Dresselhaus, *Journal of Physics: Condensed Matter: an Institute of Physics journal* **28**, 353002 (2016).
- [64] L. Sun, J. Yan, D. Zhan, L. Liu, H. Hu, H. Li, B. K. Tay, J.-L. Kuo, C.-C. Huang, D. W. Hewak, P. S. Lee, and Z. X. Shen, *Physical Review Letters* **111**, 126801 (2013).
- [65] H. Li, Q. Zhang, C. C. R. Yap, B. K. Tay, T. H. T. Edwin, A. Olivier, and D. Baillargeat, *Advanced Functional Materials* **22**, 1385 (2012).
- [66] Y. Zhao, X. Luo, H. Li, J. Zhang, P. T. Araujo, C. K. Gan, J. Wu, H. Zhang, S. Y. Quek, M. S. Dresselhaus, and Q. Xiong, *Nano Letters* **13**, 1007 (2013).
- [67] J. L. Verble and T. J. Wieting, *Physical Review Letters* **25**, 362 (1970).
- [68] B. Chakraborty, A. Bera, D. V. S. Muthu, S. Bhowmick, U. V. Waghmare, and A. K. Sood, *Physical Review B* **85** (2012), 10.1103/PhysRevB.85.161403.
- [69] S. Mignuzzi, A. J. Pollard, N. Bonini, B. Brennan, I. S. Gilmore, M. A. Pimenta, D. Richards, and D. Roy, *Physical Review B* **91** (2015), 10.1103/PhysRevB.91.195411.

- [70] B. R. Carvalho, L. M. Malard, J. M. Alves, C. Fantini, and M. A. Pimenta, *Physical Review Letters* **114**, 136403 (2015).
- [71] H.-P. Komsa and A. V. Krasheninnikov, *The Journal of Physical Chemistry Letters* **3**, 3652 (2012).
- [72] S.-H. Su, Y.-T. Hsu, Y.-H. Chang, M.-H. Chiu, C.-L. Hsu, W.-T. Hsu, W.-H. Chang, J.-H. He, and L.-J. Li, *Small* **10**, 2589 (2014).
- [73] J. Mann, Q. Ma, P. M. Odenthal, M. Isarraraz, D. Le, E. Preciado, D. Barroso, K. Yamaguchi, G. von Son Palacio, A. Nguyen, T. Tran, M. Wurch, A. Nguyen, V. Klee, S. Bobek, D. Sun, T. F. Heinz, T. S. Rahman, R. Kawakami, and L. Bartels, *Advanced Materials* **26**, 1399 (2014).
- [74] H. Li, Q. Zhang, X. Duan, X. Wu, X. Fan, X. Zhu, X. Zhuang, W. Hu, H. Zhou, A. Pan, and X. Duan, *Journal of the American Chemical Society* **137**, 5284 (2015).
- [75] S. J. Sandoval, D. Yang, R. Frindt, and J. Irwin, *Physical Review B* **44**, 3955 (1991).
- [76] J. Ribeiro-Soares, R. M. Almeida, E. B. Barros, P. T. Araujo, M. S. Dresselhaus, L. G. Cançado, and A. Jorio, *Physical Review B* **90** (2014), 10.1103/PhysRevB.90.115438.
- [77] A. Molina-Sánchez and L. Wirtz, *Physical Review B* **84** (2011), 10.1103/PhysRevB.84.155413.
- [78] D. Bersani, P. P. Lottici, and X.-Z. Ding, *Applied Physics Letters* **72**, 73 (1998).
- [79] G. L. Frey, R. Tenne, M. J. Matthews, M. S. Dresselhaus, and G. Dresselhaus, *Physical Review B* **60**, 2883 (1999).
- [80] L. G. Cançado, A. Jorio, E. H. M. Ferreira, F. Stavale, C. A. Achete, R. B. Capaz, M. V. O. Moutinho, A. Lombardo, T. S. Kulmala, and A. C. Ferrari, *Nano Letters* **11**, 3190 (2011).
- [81] C. Thomsen and S. Reich, *Physical Review Letters* **85**, 5214 (2000).
- [82] P. Giannozzi, O. Andreussi, T. Brumme, O. Bunau, M. Buongiorno Nardelli, M. Calandra, R. Car, C. Cavazzoni, D. Ceresoli, M. Cococcioni, N. Colonna, I. Carnimeo, A. Dal Corso, S. de Gironcoli, P. Delugas, R. A. DiStasio, A. Ferretti, A. Floris, G. Fratesi, G. Fugallo, R. Gebauer, U. Gerstmann, F. Giustino, T. Gorni, J. Jia, M. Kawamura, H.-Y. Ko, A. Kokalj, E. Küçükbenli, M. Lazzeri, M. Marsili, N. Marzari, F. Mauri, N. L. Nguyen, H.-V. Nguyen, A. Otero-de-la Roza, L. Paulatto, S. Poncé, D. Rocca, R. Sabatini, B. Santra, M. Schlipf, A. P. Seitsonen, A. Smogunov, I. Timrov, T. Thonhauser, P. Umari, N. Vast, X. Wu, and S. Baroni, *Journal of Physics. Condensed Matter : an Institute of Physics Journal* **29**, 465901 (2017).
- [83] T. Sohler, M. Calandra, and F. Mauri, *Physical Review B* **96** (2017), 10.1103/PhysRevB.96.075448.
- [84] D. R. Hamann, *Physical Review B* **88**, 1544 (2013).
- [85] M. J. van Setten, M. Giantomassi, E. Bousquet, M. J. Verstraete, D. R. Hamann, X. Gonze, and G.-M. Rignanese, *Computer Physics Communications* **226**, 39 (2018).
- [86] R. Loudon, *Advances in Physics* **50**, 813 (2001).
- [87] H. Kuzmany, *Solid-state spectroscopy: An introduction*, 2nd ed. (Springer, Heidelberg and New York, 2009).

Supporting Information: The Raman Spectrum of Janus Transition Metal Dichalcogenide Monolayers WSSe and MoSSe

S1. SYMMETRY AND CHARACTER TABLES

Figure S1 shows the Brillouin Zone of the Janus TMDs. The zone centre Γ point has the same symmetry as the crystal, while the \mathbf{K} and \mathbf{M} high symmetry points are subgroups with C_3 and C_s symmetries, respectively. Tables S1-S3 list the character table for each of these point groups. Table S4 shows the back-scattering geometry polarization selection rules.

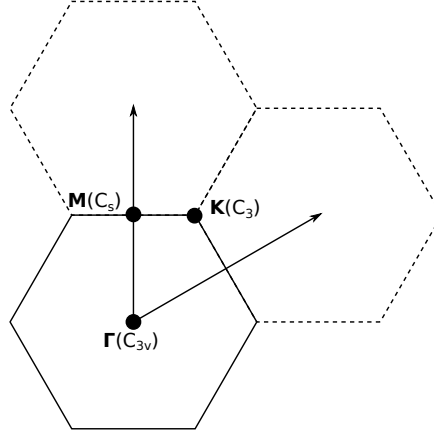


FIGURE S1. Groups and subgroups for the high symmetry points of the Brillouin Zone of Janus TMDs.

C_{3v}	E	$2C_3(z)$	$3\sigma_v$	linear functions, rotations	quadratic functions
A_1	+1	+1	+1	z	$x^2 + y^2, z^2$
A_2	+1	+1	-1	R_z	-
E	+2	-1	0	$(x, y) (R_x, R_y)$	$(x^2 - y^2, xy) (xz, yz)$

TABLE S1. Character table for point group C_{3v} .

C_3	E	$C_3(z)$	$(C_3)^2$	linear functions, rotations	quadratic functions
A	+1	+1	+1	z, R_z	$x^2 + y^2, z^2$
1E	+1	$+e^{2\pi i/3}$	$+e^{-2\pi i/3}$	$x + iy, R_x + iR_y$	$(x^2 - y^2, xy) (yz, xz)$
2E	+1	$+e^{-2\pi i/3}$	$+e^{2\pi i/3}$	$x - iy, R_x - iR_y$	$(x^2 - y^2, xy) (yz, xz)$

TABLE S2. Character table for point group C_3 .

C_s	E	σ_h	linear functions, rotations	quadratic functions
A'	+1	+1	x, y, R_z	x^2, y^2, z^2, xy
A''	+1	-1	z, R_x, R_y	yz, xz

TABLE S3. Character table for point group C_s .

	$A_1(\text{LO})$	$A_1(\text{TO})$	$E(\text{LO})$	$E(\text{TO})$
$-\text{Z}(\text{XX})\text{Z}$	x	-	-	x
$-\text{Z}(\text{XY})\text{Z}$	-	-	-	x
$-\text{Z}(\text{YY})\text{Z}$	x	-	-	x

TABLE S4. **Polarization selection rules for first-order modes.** The convention A(BC)D indicates A the direction of propagation of incident beam, B the polarization direction of the incident beam, C the polarization direction of the scattered light and D the direction of propagation of the scattered light.

S2. PHONON BANDGAPS

Phonon band structure of Janus TMD monolayers (Figure 1b and 1c, main text) reveals the gap of inaccessible phonons that separates acoustic from optical bands. WSSe and MoSSe exhibit $\Delta_{\text{TO}_1-\text{LA}}^{\text{WSSe}} \approx 46 \text{ cm}^{-1}$ and $\Delta_{\text{TO}_1-\text{LA}}^{\text{MoSSe}} \approx 24 \text{ cm}^{-1}$ bandgaps, respectively. Forbidden phonon energies occur also between optical bands (phonon bandgaps of $\Delta_{\text{TO}_2-\text{ZO}_1}^{\text{WSSe}} \approx 46 \text{ cm}^{-1}$ for WSSe and $\Delta_{\text{TO}_2-\text{ZO}_1}^{\text{MoSSe}} \approx 53 \text{ cm}^{-1}$ for MoSSe).

S3. PHOTOLUMINESCENCE OF WSSe AND MoSSe

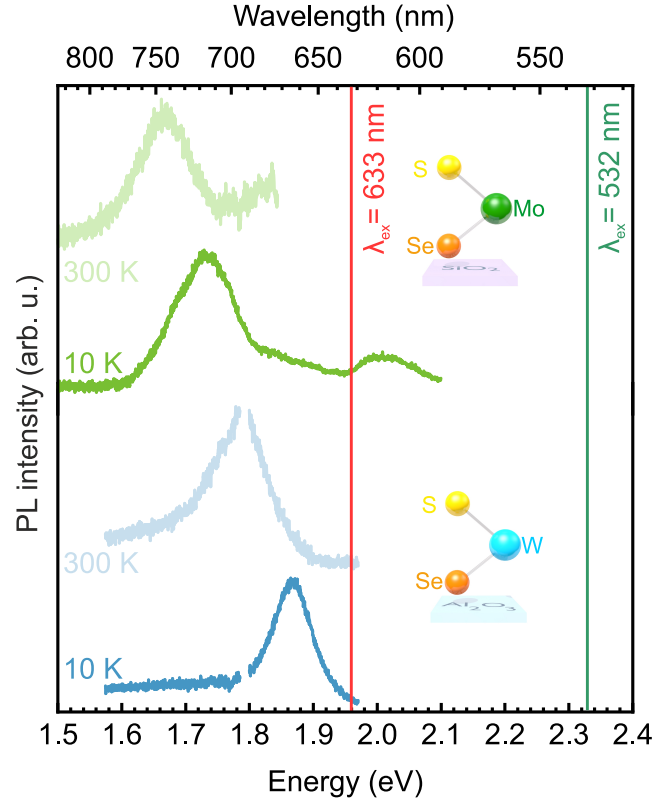


FIGURE S2. **Photoluminescence spectra of Janus WSSe and MoSSe monolayers at 10 K and 300 K.** Laser excitation wavelength $\lambda_{\text{ex}} = 633 \text{ nm}$ is close to A exciton resonance in WSSe (dark blue) and to B exciton resonance in MoSSe (dark green).